Electronic Supplementary Material (ESI) for Energy & Environmental Science.
This journal is © The Royal Society of Chemistry 2024
Electronic Supporting Information

Photoelectrochemical nitrate denitrification towards acidic ammonia synthesis on copper-decorated black silicon

Yuchan Li,[a] Qi Zhang,[a] Huan Dai,[a] Dong He,[a] Zunjian Ke*[a], Xiangheng Xiao*[a,]

[a]School of Physics and Technology, Key Lab of Artificial Micro- and Nano-Structures of Ministry of Education, Wuhan University, Wuhan 430072, China

E-mail: zjke@whu.edu.cn; xxh@whu.edu.cn

Methods

Materials

Silicon wafers were purchased from Zhejiang Lijing Silicon Material Co., Ltd. Chemicals hydrofluoric acid (HF, AR), silver nitrate ($AgNO_3$, AR), hydrogen peroxide (H_2O_2, AR), nitric acid (HNO_3, AR), sulfuric acid (H_2SO_4, AR), sodium hydroxide (NaOH, 96.0%), potassium hydroxide (KNO_3, AR), ammonium chloride (NH_4Cl, 99.9%), salicylic acid ($C_7H_6O_3$, 99.5%) and sodium citrate ($C_6H_5Na_3O_7$, AR) were purchased from Sinopharm Chemical Reagent Co., Ltd. (Shanghai, China). Chemicals copper(II) chloride dihydrate ($CuCl_2 \cdot 2H_2O$, AR), ammonium chloride-^{15}N (^{15}N-NH_4Cl, 98.5%, 99atom%), and sodium nitroferricyanide dihydrate ($C_5FeN_6Na_2O \cdot 2H_2O$, 99.0%) were purchased from Aladdin Co., Ltd. Sodium hypochlorite solution (NaClO, available chlorine 6~14%) and potassium nitrate-^{15}N ($K^{15}NO_3$, 98.5%, 99atom%) were purchased from Shanghai Macklin Biochemical Technology Co., Ltd. All chemicals are analytical grade and used without additional purification. Ultrapure water (18.25 MΩ cm) was used in all experiments.

Fabrication of Si NWs photocathode

The Si NWs were prepared by a metal-assisted chemical etching of p-Si wafer [1]. The backside of the silicon wafer (p-Si) was initially coated with polyimide to prevent etching, followed by ultrasonic cleaning using acetone and deionized water for 15 min to eliminate impurities. Subsequently, the p-Si was immersed in a 5% HF solution for 90 s to etch the surface silica layer. Afterwards, it was submerged in a 10% HF solution containing 0.02 M $AgNO_3$ for 1 min to facilitate silver particle deposition on its surface, resulting in Ag/p-Si formation. To obtain silicon nanoarrays (Si NWs), the Ag/p-Si samples were then subjected to immersion in a mixture of 10% HF and 30% H_2O_2 (in a volume ratio of 10:1) for 10 min, followed by subsequent immersion in 35% HNO_3 for an additional duration of 15 min to remove any remaining silver residues. Finally, Si photoelectrodes were prepared following the subsequent steps: (1) immersing Si in 5 wt% HF for 30 s to eliminate SiO_2; (2) applying a Ga-In alloy on the backside of Si to facilitate ohmic contact formation; (3) coating a conductive silver paste onto a copper coil with conductivity; (4) securely bonding the backside of Si with the Ga-In alloy using the conductive copper coil coated with the conductive silver paste; and (5) threading the tail of the copper coil through a quartz tube to establish electrical contact. Subsequently, (6) Loctite 9462 epoxy resin was employed for encapsulating the photo-electrode assembly, which was then dried overnight at room temperature.

Preparation of Cu-Si NWs photocathode

The Cu-Si NWs electrode was prepared by a photo-deposition method. First, Cu NPs was deposited onto Si NWs photocathode by photo-reduction in 5.0 mM $CuCl_2$ aqueous solution containing 0.40 M methanol as a hole scavenger, illuminated with AM 1.5G light at 100 mW/cm^2 for 2 min. Then the Cu-Si NWs electrode was immersed in deionized water to remove any residual Cl^- on the surface, and allow it to dry naturally in a vacuum drying oven.

Characterizations

The morphologies of samples were visualized by scanning electron microscopy (SEM) using a FEI Quanta 450 SEM operated at 5 kV. The high-resolution TEM and element mapping were all carried out by JEOL JEM-ARM200 transmission electron microscope (TEM) at 200 kV. The chemical state was analyzed by X-ray photoelectron spectroscopy (XPS, Thermo Fisher Scientific ESCALAB250Xi). The crystalline structure of catalysts was characterized by a Rigaku SmartLab-3kW Powder X-Ray Diffractometer (XRD) with Cu Kα radiation (λ = 1.540598 Å) operating at 30 kV and 30 mA. The Raman spectra were collected through Horiba HR Evolution. The reflectance spectra were recorded by using UV–vis spectrophotometers (PerkinElmer 1050+). The time-resolved photoluminescence (TRPL) spectra were measured by FLS980 fluorescence spectrophotometer (Edinburgh Instruments Ltd., UK.) at room temperature. UV photoelectron spectra (UPS) was performed by PHI 5000 VersaProbe III with He I source (21.22 eV) under an applied negative bias of 10.0 V.

PEC measurements

PEC measurements were carried out in a three-electrode electrochemical cell connected to an electrochemical workstation CHI 760E under AM 1.5G simulated sunlight of 100 mW cm^{-2}. The simulated solar illumination was obtained from a 300 W Xenon lamp (Newport model 66902) with an AM 1.5G filter. The photocathodes (cross-sectional area = 0.25 cm^2) were front-side illuminated and used as the work electrode (WE) while Ag/AgCl electrode and carbon rod were used as the reference electrode (RE) and counter electrode (CE), respectively. The PEC performance was recorded in an H-cell, in which 30 mL cathode and 30 mL anode chambers were separated by an anion-exchange membrane (Nafion 115, N115). The conversion between the potentials versus Ag/AgCl and the potentials versus RHE was performed using the following equation:

$$E\ (V\ vs.\ RHE) = E\ (V\ vs.\ Ag/AgCl) + 0.059\times pH + 0.197 \quad (1)$$

The cathode chamber was filled with 25 mL, 0.5 M H_2SO_4 solution and dissolved with 100 mM KNO_3 and the anode chamber electrolyte was filled with 25 mL of 0.5 M H_2SO_4 solution. The reaction temperature for all photoanodes is maintained at 25 ℃. Before every *J-t* measurement,

the photocathode was immersed in 1% HF for 30 s to remove SiO_2. The photocurrent was recorded at a scan rate of 20 mV s^{-1} with and without the presence of 100 mM KNO_3. IPCE were tested using a Xenon lamp (Newport model 66902) with a grating monochromator (Newport model 74125) and an optical power meter (Newport model) at a bias of −0.4 V *vs.* RHE from 400 to 1000 nm, which calculated by Supplementary Equation [1]:

$$\text{IPCE} = \frac{J\left(mA^{-2}\right) \times 1240\ (V\ nm)}{P\left(mW\ cm^{-2}\right) \times \lambda\ (nm)} \times 100 \tag{2}$$

where J is the photocurrent density, λ is the wavelength of the incident light, and P is the illumination intensity at different wavelengths. The incident photo-to-NH_4^+ efficiency was calculated by Supplementary Equation [2]:

$$\text{Incident photo-to-}NH_4^+\text{ conversion efficiency} = IPCE \times f_{NH_4^+} \tag{3}$$

Where $f_{NH_4^+}$ is the Faradaic efficiency of NH_4^+.

Applied bias photon-to-current efficiency (ABPE) was given by the following equation:

$$\text{ABPE} = \frac{J_{ph}(0.69 - V_{app})}{P_{light}} \times 100\% \tag{4}$$

where V_{app} is the applied potential versus RHE, J_{ph} is the photocurrent density (mA cm^{-2}), and P_{light} is the irradiance of the simulated sunlight (100 mW cm^{-2}).

The injection efficiency (η_{inj}) and charge separation efficiency (η_{sep}) of the photocathode were investigated using 0.5 M Na_2SO_3 as a hole scavenger. LSV curves of electrolyte solutions of 0.5 M H_2SO_4 and 0.5 M H_2SO_4 + 0.1 M KNO_3 were collected under light conditions, respectively. The η_{inj} and η_{sep} were calculated using the following equations:

$$\eta_{inj} = \frac{J_{H_2O}}{J_{Na_2SO_3}} \times 100\% \tag{5}$$

$$\eta_{sep} = \frac{J_{Na_2SO_3}}{J_{abs}} \times 100\% \tag{6}$$

where J_{H_2O} and $J_{Na_2SO_3}$ are the photocurrent densities obtained in 0.5 M H_2SO_4 without and with 0.1 M KNO_3, respectively. Absorption photocurrent density (J_{abs}) was the expected photocurrent density when absorbed photons are completely converted into current:

$$J_{abs} = \int \frac{\lambda}{1240} \Phi_\lambda [1 - 10^{-A}]\, d\lambda \tag{7}$$

Where λ, Φ_λ, and A stand for the photo wavelength, photo flux of solar spectrum (AM 1.5 G), and the absorbance of photocathode, respectively.

Mott-Schottky plots were derived from impedance-potential tests conducted at a frequency of

1000 Hz in dark.

Ammonia detection and Faradaic efficiency calculation

Characterization of NO_3^- reduction reaction liquid product was employed by nuclear magnetic resonance technique (NMR, Bruker BioSpin AG, AVANCE NEO 400) and ion chromatography (Wayeal, IC 6100). The quantification of produced ammonia was detected by the indophenol blue method. After the *J-t* test (t = 3 h), the generated NH_4^+ products were detected by the indophenol blue method on a UV-Vis 2700 spectrophotometer (Shimadzu, Japan) of an integrating sphere at a wavelength of 500 to 800 nm. In a typical indophenol blue method,[3] 2 mL of electrolyte was extracted, and 2 mL of 0.55 M NaOH solution (containing 5.0 wt.% salicylic acid and 5.0 wt.% sodium citrate), 200 μL of $C_5FeN_6Na_2O$ (10 g L^{-1}), and 200 μL of 0.05 M NaClO were added. After storage at room temperature for 2 h in dark, the absorbance of the mixed solution was measured at a wavelength of 665 nm. NH_4^+ concentration was calculated by calibrating the concentration-absorbance curve (Figure S9) in 0.5 M H_2SO_4 solution using ammonium chloride (NH_4Cl) as a standard sample. The NH_4Cl solutions with various concentrations (2, 5, 10, 20, 50, and 100 μg/mL) were prepared for UV-vis tests according to the above steps. The standard concentration curve was obtained via a linear fitting of various concentrations and corresponding absorbances. The ammonia concentrations obtained from the above standard curve concentrations were used to calculate the Faradaic efficiencies (FE) of the ammonia produced from NO_3^- reduction. The total reactions of nitrate reduction were shown in the following:

$$NO_3^- + 8e^- + 10H^+ = NH_4^+ + 3H_2O$$

Therefore, the FEs of NH_4^+ produced from NO_3^- were calculated according to the equations:

$$\text{Faradaic efficiency (\%)} = \frac{n \times NH_4^+ \; concentrastion\left(\frac{mol}{L}\right) \times F\left(\frac{C}{mol}\right) \times V\,(L)}{Q\,(C)} \times 100 \qquad (8)$$

where n is 8, F is the Faraday constant (96485), V is electrolyte volume, and Q is the total charge passed through the photoelectrodes.

Ammonia quantitation by ^{1}H NMR

The produced NH_4^+ was also quantified by ^{1}H nuclear magnetic resonance (^{1}H NMR) measurement. D_2O was employed as a spin-lock field and maleic acid (400 ppm) was used as the internal standard. The calibration curve was obtained using the concentration of NH_4^+ versus the peak area ratio between NH_4^+ and maleic acid. The electrolyte obtained was diluted five times using 400 ppm maleic acid. Then, 60 μL D_2O was added to 540 μL treated solution for further characterization by ^{1}H NMR.

^{15}N isotope labeling experiments

The ^{15}N isotope labeling experiment was carried out to track the path of N in produced ammonia. To demonstrate that the nitrogen atoms in the produced ammonia were derived from NO_3^- reduction, the 0.5 M H_2SO_4 with 100 mM $K^{14}NO_3$ and $K^{15}NO_3$ was used as the electrolyte for photo-electrolysis, respectively.

***In-situ* attenuated total reflection Fourier transformed infrared (ATR−FTIR) test**

In-situ FTIR spectroscopy experiments were performed using a customized photoelectrochemical cell integrated into a Nicolet iS50 (Thermo Fischer Scientific) FTIR spectrometer, which was equipped with a mercury-cadmium-telluride (MCT) detector cooled by liquid nitrogen. The working electrode, counter electrode, and reference electrode utilized were the self-supported catalysts electrode, Pt wire, and Ag/AgCl electrode, respectively (see Supplementary Fig. 21). After collecting the spectrum under open circuit potential as background, *j–t* tests were conducted to collect infrared absorption spectra at different potentials, with each potential lasting for 2 min for spectrum collection.

Density Functional Theory (DFT) Calculation

The DFT simulations in this study were performed using the CASTEP code, which is implemented in the Materials Studios package. The electron exchange-correlation potential was calculated using the Perdew−Burke−Ernzerhof (PBE) functional of the generalized gradient approximation (GGA). Ultrasoft pseudopotentials were utilized with a kinetic energy cutoff of 500 eV for the plane-wave basis set. The Brillouin zone integration was sampled using a 1 × 1 × 1 Monkhorst−Pack mesh k-point. Energetic and force tolerances were set to 1×10^{-5} eV/atom and 0.003 eV/ Å, respectively. A Cu (200) plane and Si (100) plane with a vacuum region of 15 Å along the Z-axis was constructed based on the XRD and HRTEM results for calculation. The free energy (ΔG) calculations for each elementary step were based on the standard hydrogen electrode model, which can be expressed as

$$\Delta G = \Delta E + \Delta E_{ZPE} - T\Delta S$$

where ΔE and ΔS represent the changes in reaction energy and entropy, respectively, and ΔE_{ZPE} denotes the disparity in zero-point energy between the adsorbed and gas phase molecules.

Supplementary figures and tables

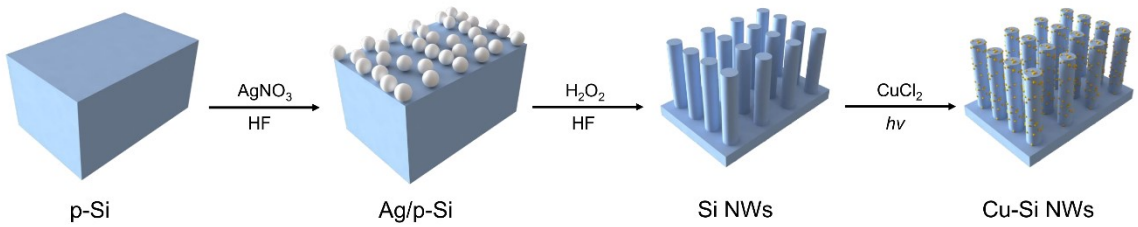

Fig. S1. Schematic illustration for the fabrication of Cu-Si NWs photoelectrode.

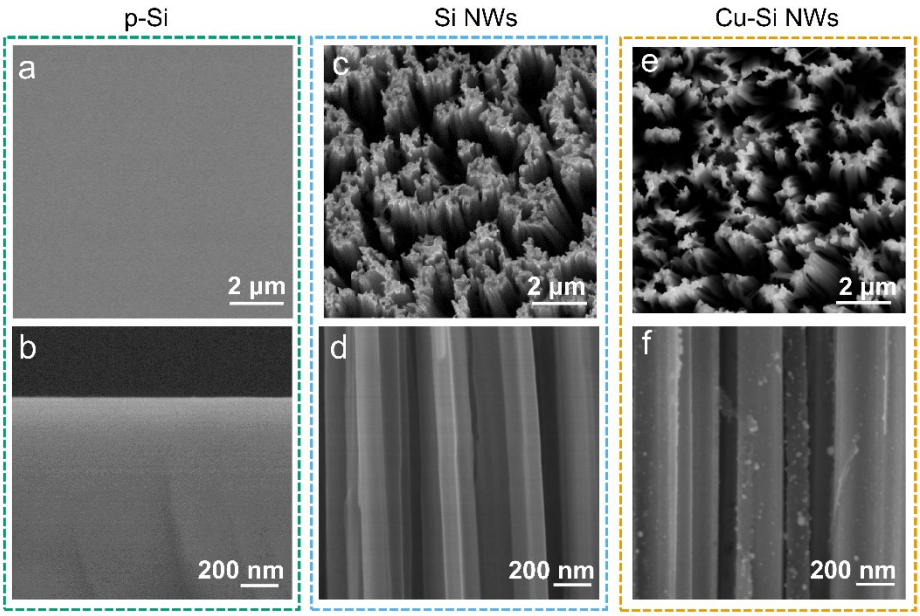

Fig. S2. Top-view SEM images of (a) planar Si, (c) Si NWs, (e) Cu-Si NWs, and their corresponding side-view images (b, d, f). In **Fig. S2a-b**, the surface and cross section of the etched silicon wafer exhibited smooth features. Following the MACE process, as showed in **Fig. S2c-d** the resulting Si NWs displayed a porous structure on the surface and a nanoarray structure on the side-view. After preparing Cu-Si NWs using the photo-deposition method, it was observed that Cu NPs were uniformly loaded onto Si NWs without any apical aggregation in **Fig. S2e-f**.

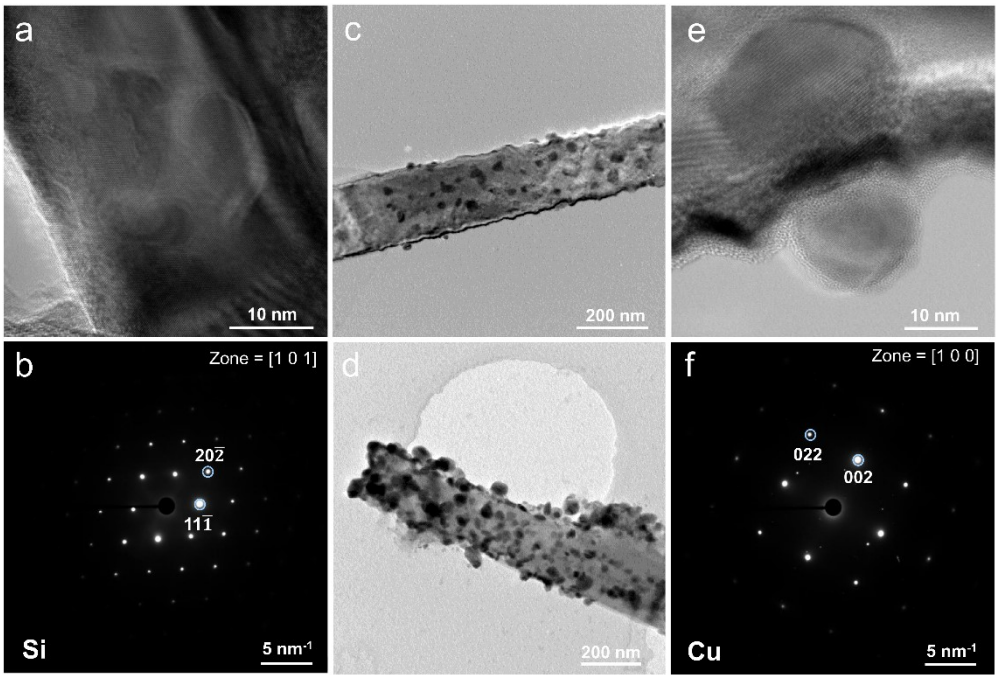

Fig. S3. High-resolution TEM images (a) and corresponding selected area electron diffraction (SAED) pattern (b) of Si NWs, indicating that it possesses a well-defined nanowire morphology and an excellent crystalline structure. TEM images (c, d), high resolution TEM images (e), and corresponding SAED pattern (f) of Cu-Si NWs. The results clearly demonstrate the homogeneous distribution of Cu nanoparticles on Si NWs and their exceptional crystalline quality.

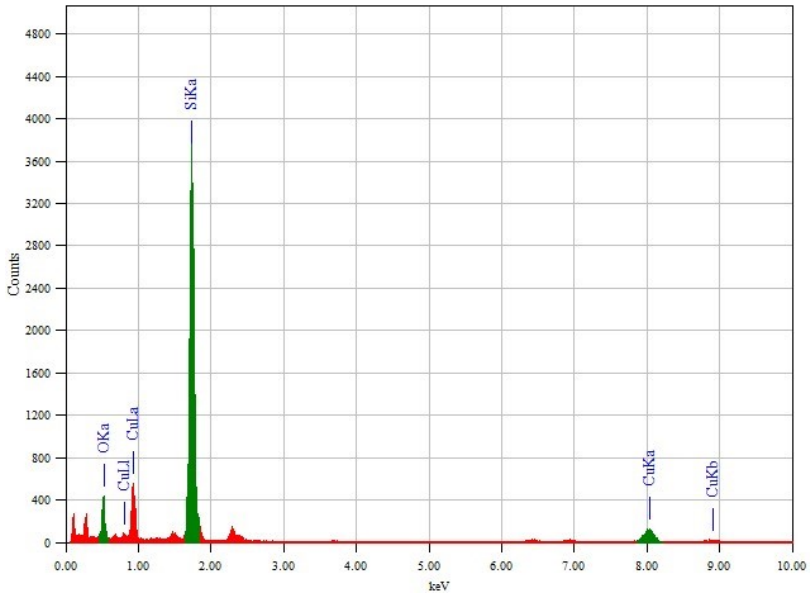

Z	Element	Family	Atomic fraction
14	Si	K	97.4%
29	Cu	K	2.6%

Fig. S4. EDS spectra and elemental quantitation of Cu-Si NWs.

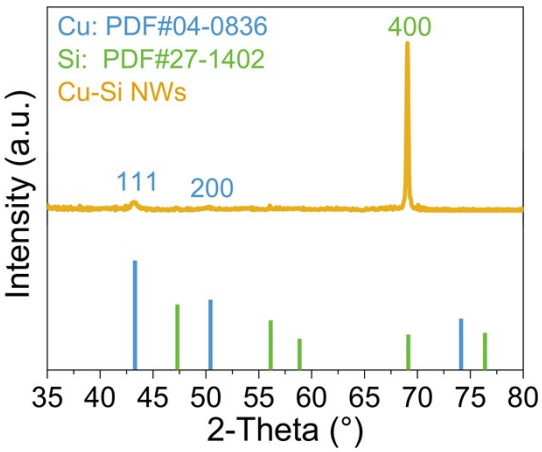

Fig. S5. XRD pattern of Cu-Si NWs.

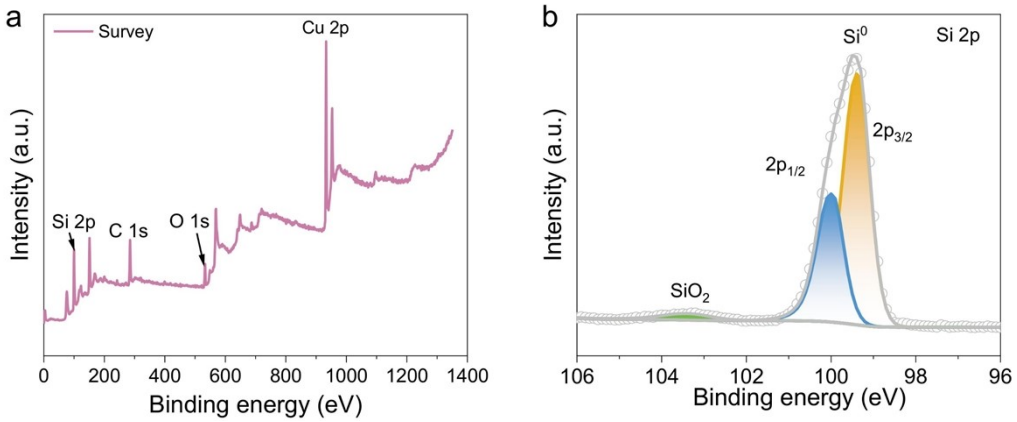

Fig. S6. XPS survey spectra (a) and Si 2p (b) of Cu-Si NWs.

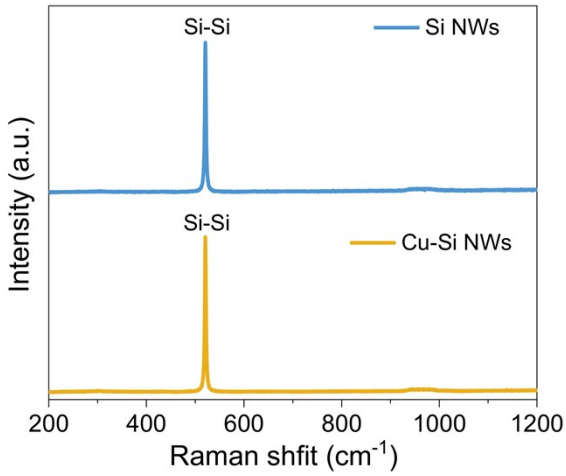

Fig. S7. Raman spectra of Si NWs and Cu-Si NWs.

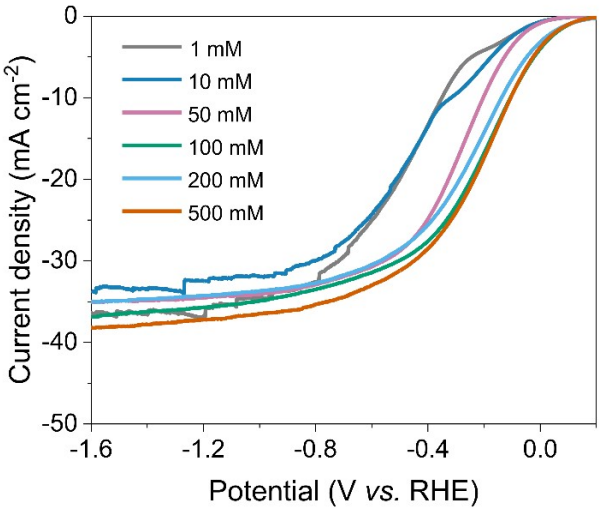

Fig. S8. *J-V* curve of Cu-Si NWs in a 0.5 M H_2SO_4 electrolyte with different concentrations of KNO_3.

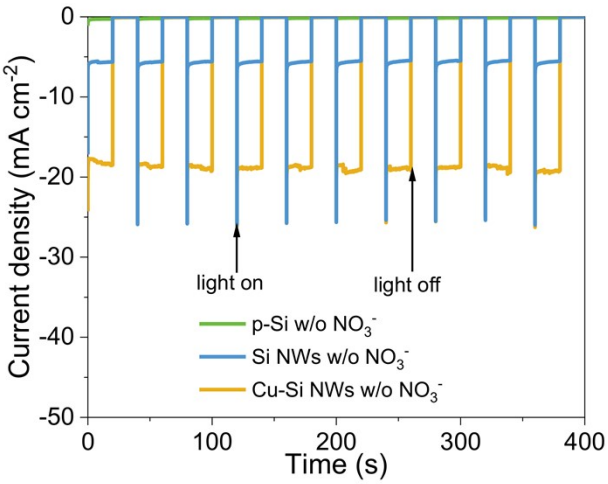

Fig. S9. Transient photocurrent responses of the photocathodes at –0.4 V *vs.* RHE in 0.5 M H_2SO_4 without NO_3^-.

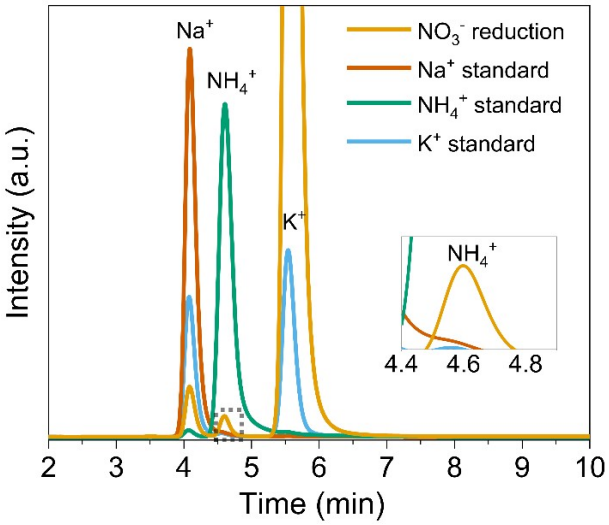

Fig. S10. Ion chromatography (IC) verification of ammonium produced from NO_3^- photo-electroreduction catalyzed by Cu-Si NWs photocathode at −0.4 V *vs.* RHE. Na^+ was from the impurity in KNO_3.

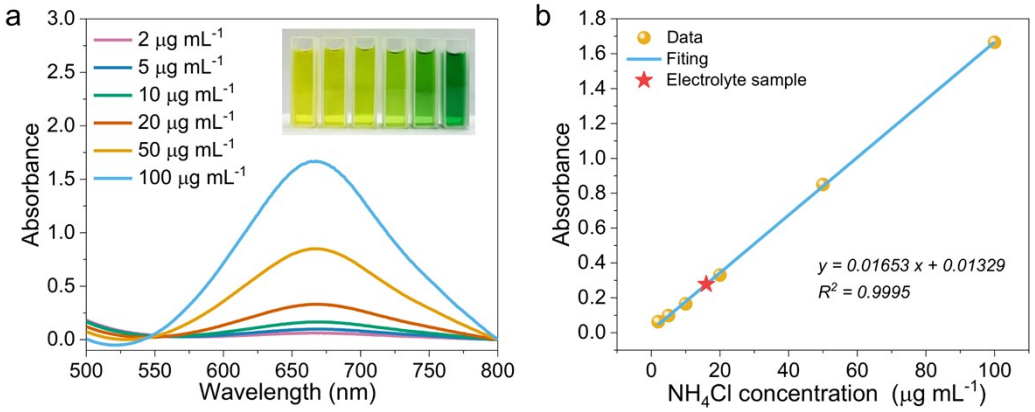

Fig. S11. The concentration-absorbance UV-vis calibration curve of NH_4^+ using different concentration of NH_4Cl solutions as standards. (a) UV–vis curves of indophenol assays with NH_4^+ ions and (b) linear fitting results of the calibration curve.

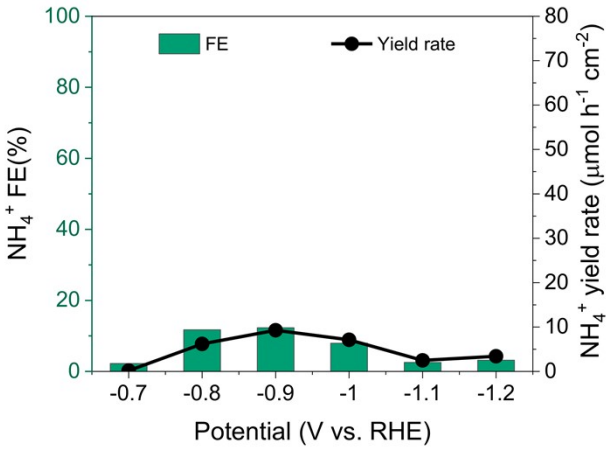

Fig. S12. The NH_4^+ FE and yield rate of p-Si photocathode in different potential. The weak catalytic activity of p-Si and its limited contribution to NH_4^+ yield was evident, resulting in sparse and challenging detection of NH_4^+ generation within the range of −0.1 to −0.6 V *vs*. RHE. Upon extending the detection range to −0.7 to −1.2 V *vs*. RHE, the low FE and yield of NH_4^+ up to 12.29% and 9.28 μmol h^{-1} cm^{-2} were observed for p-Si at −0.9 V *vs*. RHE.

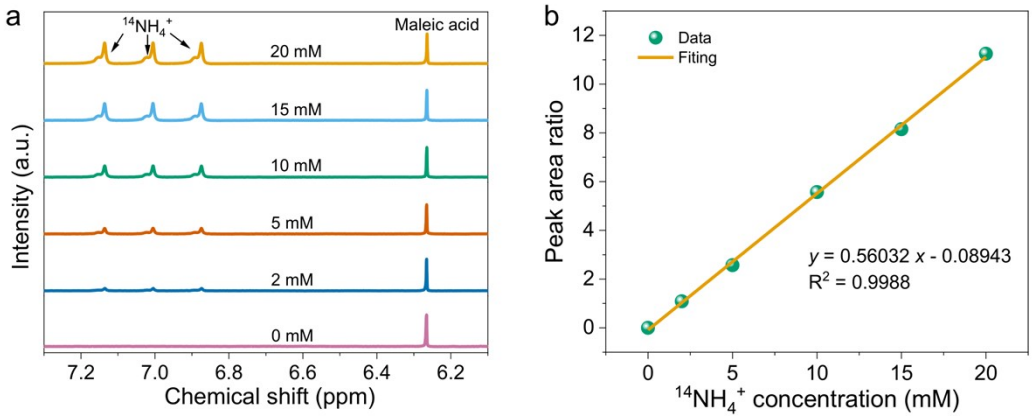

Fig. S13. Standard curve of $^{14}NH_4^+$ quantification by ^1H NMR. (a)^1H NMR spectra of ammonia-^{14}N at different concentrations and (b) the corresponding standard curve. The concentration of $^{14}NH_4^+$ and $^{15}NH_4^+$ can be quantitatively determined by ^1H NMR with external standards (maleic acid). The proton signal of maleic acid appears at δ = 6.26 ppm. The ^1H NMR spectra of $^{14}NH_4^+$ show triple peaks at δ = 6.87, 7.00, and 7.13 ppm. The calibration curve shows good linearity.

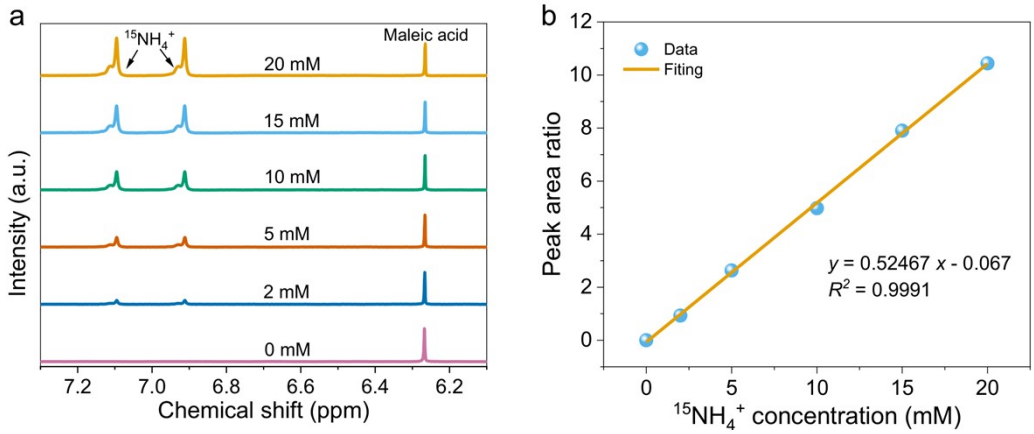

Fig. S14. Standard curve of $^{15}NH_4Cl$ quantification by ^1H NMR. (a)^1H NMR spectra of ammonia-^{15}N at different concentrations and (b) the corresponding standard curve. The concentration of $^{15}NH_4^+$ can be quantitatively determined by ^1H NMR with external standards (maleic acid). The proton signal of maleic acid appears at δ = 6.26 ppm. The ^1H NMR spectra of $^{15}NH_4Cl$ show double peaks at δ = 6.91 and 7.01 ppm. The areas of these two peaks are equivalent. The calibration curve shows good linearity.

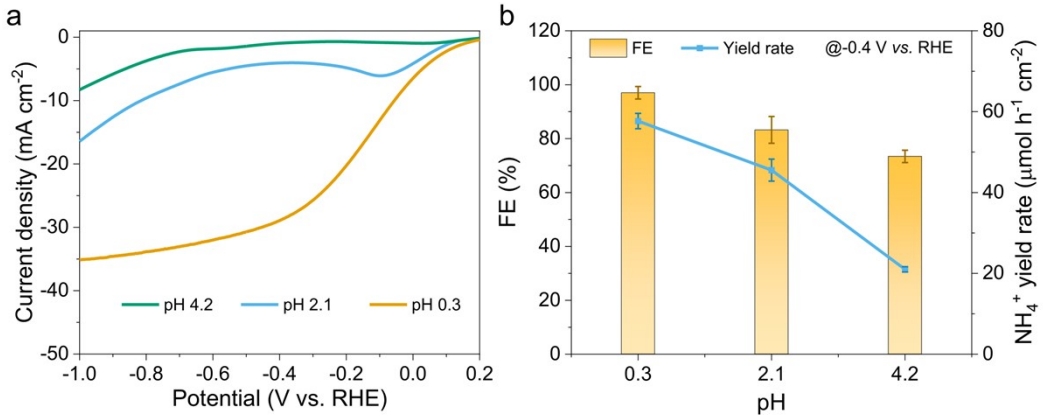

Fig. S15. PEC NO_3RR performance (a) LSV plots of Cu-Si NWs in 0.5 M H_2SO_4 with 100 mM NO_3^- (scan rate: 20 mV s^{-1}) and (b) corresponding NH_4^+ FE as well as yield rate at different pH conditions.

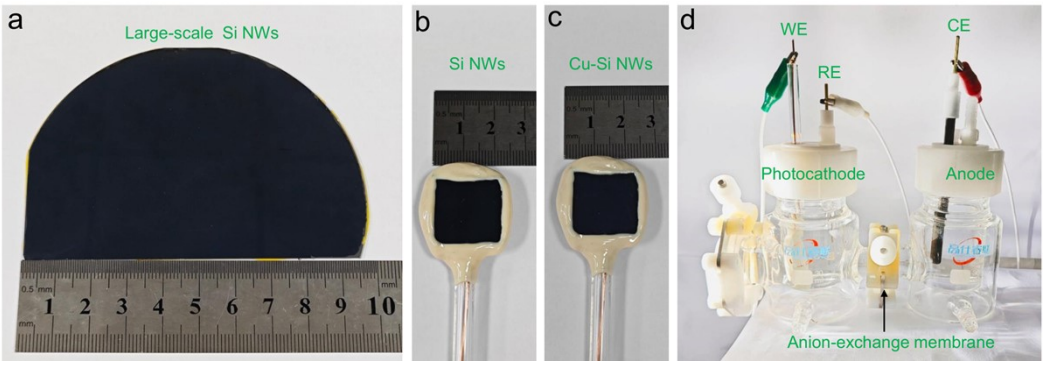

Fig. S16. (a) Preparation of large-scale black silicon (Si NWs) by metal-assisted chemical etching method. (b)Si NWs photocathode. (c) Cu-Si NWs photocathode synthesis by photodeposition. (d) Illustration of PEC device. The preparation of black silicon by metal-assisted chemical etching (MACE) was initially discovered by Malinovska *et al.*[4] and has since undergone extensive investigations. This method involves immersing a silicon wafer in a solution containing silver nitrate salt to facilitate the deposition of silver particles, followed by etching the wafer with the deposited silver particles in a mixture of hydrofluoric acid and an oxidizer to form Si NWs. Notably, this cost-effective and straightforward technique obviates the need for applying voltage current, rendering it suitable for large-scale production. Using this method, we synthesized a large-area Si NWs with a diameter of ~10 cm (**Fig. S16a)**, confirming the feasibility in scaling up the synthesis of Si NWs. The Cu-Si NWs were synthesized *via* loading Cu nanoparticles on the Si NWs prepared using MACE method. Si NWs were positioned within a transparent quartz electrolytic cell, which was filled with a deposition solution (5 mM $CuCl_2 \cdot 2H_2O$ + 0.4 M methanol) and subjected to xenon lamp irradiation for 2 min. The photo-deposition method for fabricating Cu-Si NWs is characterized by its simplicity and accessibility of equipment, enabling large-scale production. As depicted in **Fig. S16b-c**, Cu-Si NW photocathode with an area of ~4 cm^2 was successfully fabricated following the aforementioned procedure. In conclusion, by integrating wafer-scale Cu-Si NWs in series, we can, in principle, achieve the large-scale fabrication of the Cu-Si NWs photocathode.

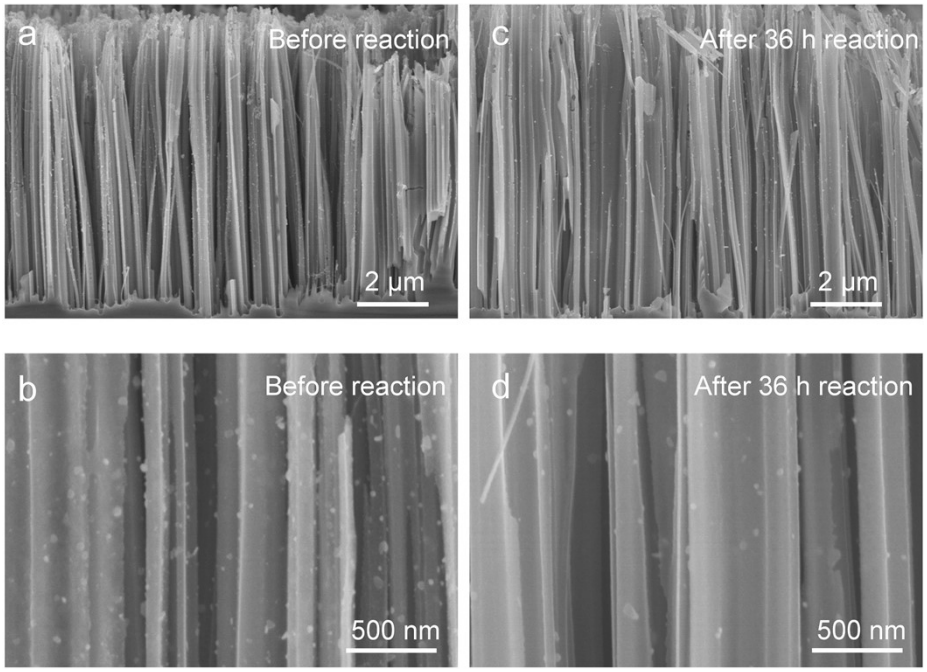

Fig. S17. Morphology comparison of Cu-Si NWs photoelectrocatalytic activity before (a, b) and after (c, d) 36-hour photoelectrolysis at –0.4 V vs. RHE. The presence of Cu nanoparticles attached to the surface of Cu-Si NWs was still observed even after 36 hours of reaction, with a slight shedding phenomenon being noticeable compared to its pre-reaction state.

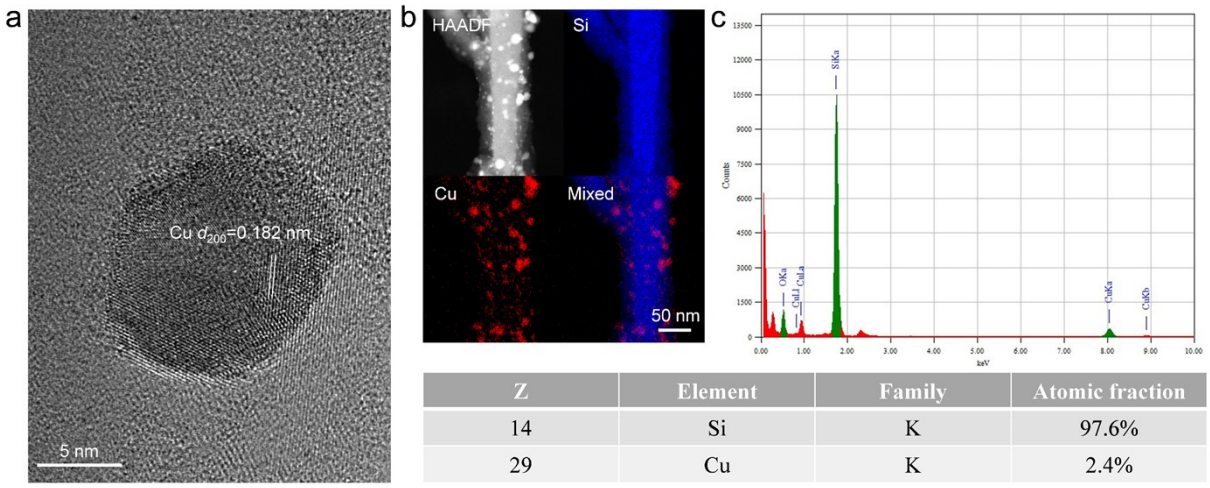

Z	Element	Family	Atomic fraction
14	Si	K	97.6%
29	Cu	K	2.4%

Fig. S18. (**a**) HRTEM image and (**b, c**) the corresponding HADDF, EDS images and elemental quantitation of Cu-Si NWs after 36-hour photoelectrolysis at –0.4 V *vs*. RHE. In **Fig. S18a**, the high-resolution transmission electron microscopy (HRTEM) image revealed that the Cu-Si NWs photocathode still exhibited good crystallinity with a cubic structure after 36 hours reaction. Further, the corresponding energy-dispersive spectroscopy (HRTEM-EDS, **Fig. S18b, c**) confirms the uniform dispersion of Cu atoms in Si NWs, and the effective Cu content was also similar to that before the reaction (**Fig. S4**).

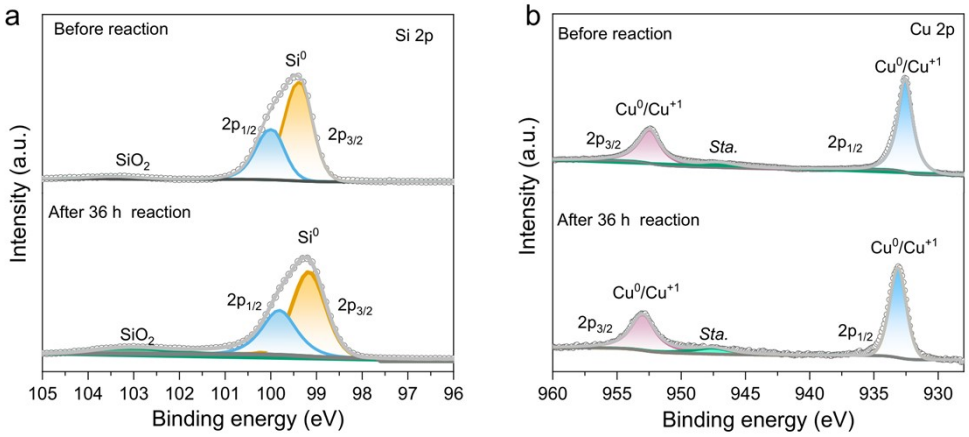

Fig. S19. High-resolution Cu 2p spectra of Cu-Si NWs photocathode (a) before and (b) after PEC NO_3RR for 36 h at −0.4 V *vs.* RHE. The XPS results indicated that the characteristic peaks of Si 2p and Cu 2p changed slightly after the 36-hour photo-electrolysis, Cu elements still existed as Cu^0, and Si element existed mainly in form of Si^0. These results revealed the great stability of Cu-Si NWs in long-term photo-electrolysis.

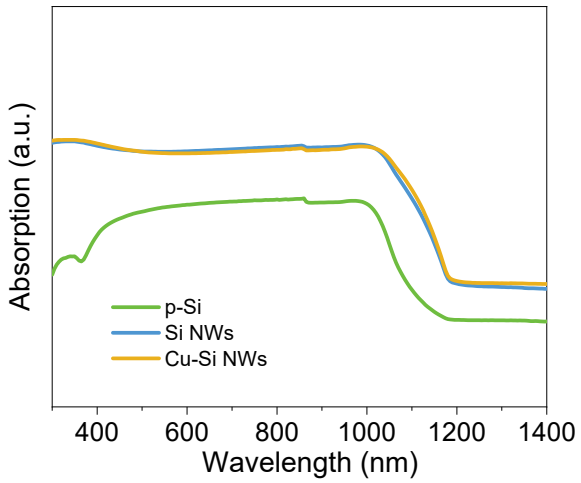

Fig. S20. UV-vis absorbance spectra of p-Si, Si NWs, and Cu-Si NWs.

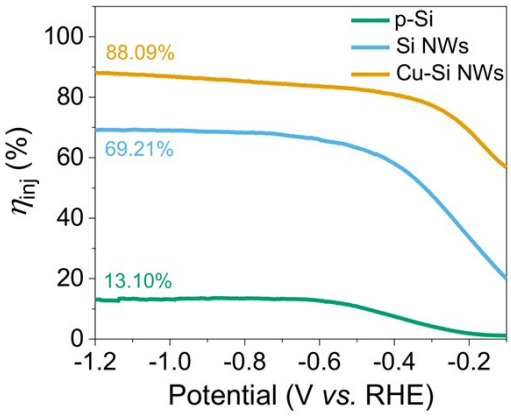

Fig. S21. Charge separation efficiency (η_{inj}) of p-Si, Si NWs, and Cu-Si NWs photocathode.

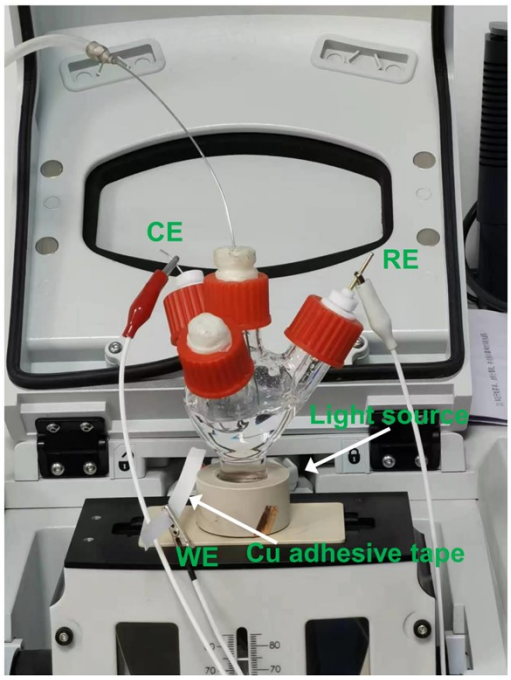

Fig. S22. Setup employed for photoelectrochemical *in situ* ATR-FTIR characterization.

Table S1. The comparable results of our work and recent works for NH_3 synthesis of photoelectrochemical (PEC) and electrochemical (EC) from NO_3^- or N_2.

Category	Photocathode/catalyst	Electrolyte (pH)	Max. current density (mA cm^{-2})	Max. FE to NH_3 (potential, V *vs.* RHE)	Max. NH_3 yield rate	Ref.
PEC for NO_3^- reduction	Cu-Si NWs	0.5 M H_2SO_4 + 0.1 M KNO_3 (pH 0.3)	−37.03	97.03% (−0.4)	65.91 μmol h^{-1} cm^{-2}	This work
	TiO_x/CdS/Cu_2ZnSnS_4	0.01 M H_2SO_4 + 0.1 M KNO_3 (pH 2)	about −2.5	89.1% (−0.1)	8.21 μmol h^{-1} cm^{-2}	[5]
	O_SiNW/Au	0.5 M K_2SO_4 + 10 mM KNO_3 (pH 3.5)	about −0.53	95.6% (−0.2)	0.39 μmol h^{-1} cm^{-2}	[6]
	CeO_2-c/$BiVO_4$	0.5 M Na_2SO_4 + 1.61 M NO_3^- (pH 7)	about −0.35	32.3% (−0.1)	1.21 μmol h^{-1} cm^{-2}	[7]
	CuPc-CeO_2	0.1 M phosphate buffer solution (PBS) KNO_3 (pH 6.87)	about −0.4	33% (−0.6)	1.16 μmol h^{-1} cm^{-2}	[8]
	CoFeMnO/$BiVO_4$	0.5 M Na_2SO_4 + 2.42 M NO_3^- (pH 7)	about −0.8	32.8% (−0.1)	0.99 μmol h^{-1} cm^{-2}	[9]
EC for NO_3^- reduction	Fe_2Co-MOF	0.05 M H_2SO_4 + 50 g L^{-1} KNO_3 (pH 1)	about −34	90.55% (−1.1)	1147.4 μmol h^{-1} mg^{-1}_{site}	[10]
	Cu NPs	0.1 M KOH + 0.1 M KNO_3 (pH 13.5)	−90	93.4% (−0.9)	115 nmol s^{-1} cm^{-2}	[11]
	RhCu M-tpp	0.5 M Na_2SO_4 + 3000 ppm NO_3^- (pH 7)	−60	84.8% (−0.2)	39.8 mmol h^{-1} g^{-1}_{cat}	[12]
	Ru SA-NC	1.0 M KOH + 0.5 M NO_3^- (pH 14)	about −200	72.8% (−0.6)	0.11 mol h^{-1} cm^{-2}	[13]
EC for N_2 reduction	Cu_3P	N_2 and Ar-saturated 0.1 M HCl (pH 1)	about −0.9	37.8% (−0.2)	1.05 μmol h^{-1} mg^{-1}	[14]
	Cu_9S_5	N_2 and Ar-saturated 0.5 M Na_2SO_4 (pH 7)	about −1.2	25.2% (−0.5)	0.6 μmol $h^{-1}cm^{-2}$	[15]
	Mo/VO_2	N_2 and Ar-saturated 0.05 M H_2SO_4 (pH 1)	about −80	32.4% (−0.5)	10.56 μmol $mg_{cat.}^{-1}$ h^{-1}	[16]
PEC for N_2 reduction	Li_xMoO_3	N_2 and Ar-saturated in 0.5 M $LiClO_4$	about −0.3	31.4% (−0.15)	0.48 μmol h^{-1} cm^{-2}	[17]
	VO_x/m-TiO_2	N_2 and Ar-saturated 0.05 M H_2SO_4 (pH 1)	about −4.5	-	0.35 μmol h^{-1} cm^{-2}	[18]
	SnO_2/MoS_2	N_2 and Ar-saturated 0.5 M Na_2SO_4 (pH 7)	about −8	40.34% (−0.3)	1.09 μmol h^{-1} mg^{-1}	[19]

Table S2. The related EIS fitting parameter for p-Si, Si NWs and Cu-Si NWs.

Photocathode	Rct	CPE-T	CPE-P
p-Si	98838	0.88821	9.4847E-7
Si NWs	23820	0.93831	1.7773E-6
Cu-Si NWs	4551	0.93402	4.4212E-6

Table S3. Biexponential decay-fitted parameters of TRPL for p-Si, Si NWs, and Cu-Si NWs photocathode.

Samples	τ_1 (ns)	τ_2 (ns)	τ_{avg} (ns)	A_1	A_2	R^2
p-Si	0.32	7.28	1.57	0.85	0.19	0.997
Si NWs	0.39	7.38	2.12	0.78	0.25	0.997
Cu-Si NWs	0.58	8.05	2.54	0.81	0.29	0.996

Table S4. The concentrations of individual components in the simulated wastewater.

Contaminant	Concentration (ppm)	Reference
COD (glucose)	1000	20, 21
Cl^-	100	20, 22
PO_4^{3-}	35	20, 22
CO_3^{2-}	35	20, 22
Ca^{2+}	4.0	20, 22
Mg^{2+}	2.5	20, 22
Fe^{3+}	1.0	20, 22
Mn^{2+}	1.0	20, 22
Zn^{2+}	0.3	20, 22

References

[1] F. Yang, J. A. Aguiar, M. Fairchild, W. Vakki, S. Younan, Y. Zhou, L. Zhuo and J. Gu, Adv. Mater. Interfaces, 2019, **6**, 1802085.

[2] L. Barrera, R. B. Chandran, *ACS Sustainable Chem. Eng*., 2021, **9**, 3688.

[3] C. Zhao, S. Zhang, M. Han, X. Zhang, Y. Liu, W. Li, C. Chen, G. Wang, H. Zhang, H. Zhao, ACS Energy Lett., 2019, **4**, 377.

[4] D. Dimova-Malinovska, M. Sendova-Vassileva, N. Tzenov, M. Kamenova, Thin Solid Films, 1997, **297**, 9.

[5] S. Zhou, K. Sun, C. Y. Toe, J. Yin, J. Huang, Y. Zeng, D. Zhang, W. Chen, O. F. Mohammed, X. Hao, R. Amal, Adv. Mater., 2022, **34**, 2201670.

[6] H.E. Kim, J. Kim, E. C. Ra, H. Zhang, Y. J. Jang, J. S. Lee, Angew. Chem. Int. Ed., 2022, **61**, e202204117.

[7] H. Bai, F. Wang, Q. Ding, W. Xie, H. Li, G. Zheng, W. Fan, Inorg. Chem., 2023, **62**, 2394.

[8] X. Li, W. Fan, Y. Bai, Y. Liu, F. Wang, H. Bai, W. Shi, Chem. Eng. J., 2022, **433**, 13322.

[9] F. Wang, Q. Ding, Y. Bai, H. Bai, S. Wang, W. Fan, Inorg. Chem. Front., 2022, **9**, 805.

[10] Y. L, S.-W. Ke, Y. G, B. Tian, L. Tang, P. Ran, Y. Zhao, J. Ma, J.-L. Zuo, M. Ding, Angew. Chem. Int. Ed., 2023, **62**, e202305246.

[11] Y. Ren, C. Yu, L. Wang, X. Tan, Z. Wang, Q. Wei, Y. Zhang, J. Qiu, J. Am. Chem. Soc., 2022, **144**, 10193.

[12] J. Zhou, Y. Xiong, M. Sun, Z. Xu, Y. Wang, P. Lu, F. Liu, F. Hao, T. Feng, Y. Ma, J. Yin, C. Ye, B. Chen, S. Xi, Y. Zhu, B. Huang, Z. Fan, P. Natl. Acad. Sci. USA., 2023, **120**, e2311149120.

[13] Z. Ke, D. He, X. Yan, W. Hu, N. Williams, H. Kang, X. Pan, J. Huang, J. Gu, X. Xiao, ACS Nano, 2023, **17**, 3483.

[14] Q. Liu, Y. Lin, S. Gu, Z. Cheng, L. Xie, S. Sun, L. Zhang, Y. Luo, A. A. Alshehri, M. S. Hamdy, Q. Kong, J. Wan, X. Sun, Nano Res., 2022, **15**, 7134.

[15] H.S. Kim, J. Choi, J. Kong, H. Kim, S.J. Yoo, H.S. Park, ACS Catal., 2021, **11**, 435.

[16] M. Xie, F. Dai, H. Guo, P. Du, X. Xu, J. Liu, Z. Zhang, X. Lu, Adv. Energy Mater., 2023, **13**, 2203032.

[17] Y. Mao, H. Zhang, W. Jiang, R. Zhao, Y. Liu, Z. Wang, P. Wang, Z. Zheng, K. Song, W. Wei, Y. Dai, J.H. He, H. Cheng, B. Huang, Nano Energy, 2022, **102**, 107639.

[18] Y. Jia, J. Gao, Z. Xiao, Z. Tian, Y. Xia, C. Wang, ACS Appl. Mater. Interfaces, 2023, **15**, 26111.

[19] H. Yang, C. Nan, N. Gao, W. Zhou, F. Gao, D. Dong, D. Dou, Y. Liu, Z. Liang, D. Yang,

Electrochim. Acta, 2022, **430**, 141086.

[20] K. Liu, H. Li, M. Xie, P. Wang, Z. Jin, Y. Liu, M. Zhou, P. Li, G. Yu, *J. Am. Chem. Soc.,* 2024, 146, 7779.

[21] W. Somasiri, X.-F. Li, W.-Q. Ruan, C. Jian, *Bioresource Technol.,* 2008, **99**, 3692.

[22] R. Chauhan, V.C. Srivastava, Chem. Eng. Sci., 2022, **247**, 117025.